Journal of Power Sources 273 (2015) 128–135

Contents lists available at ScienceDirect

Journal of Power Sources

journal homepage: www.elsevier.com/locate/jpowsour

One-step solution-combustion synthesis of complex spinel titanate flake particles with enhanced lithium-storage properties

Xue Li, Qian Xiao, Bo Liu, Huangchang Lin, Jinbao Zhao*

State Key Lab of Physical Chemistry of Solid Surfaces, Department of Chemistry, Collaborative Innovation Center of Chemistry for Energy Materials, College of Chemistry and Chemical Engineering, Xiamen University, Xiamen 361005, China

HIGHLIGHTS

- Fast solution-combustion in few minutes is developed to prepare complex spinel titanate electrodes for the first time.
- Combustion synthesis in liquid phase ensures excellent homogeneity of the product with a porous surface area.
- The synthesized electrodes exhibited great cycling stability and high rate performance even at 2000 mA g^{-1} for 200 cycles.

GRAPHICAL ABSTRACT

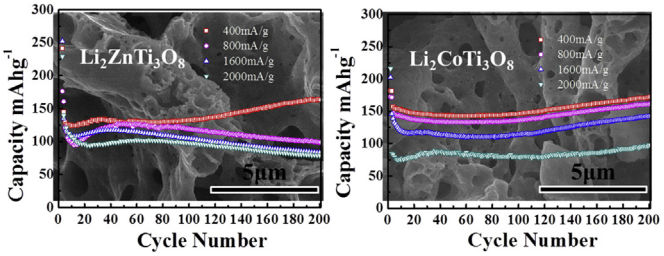

ARTICLE INFO

Article history:
Received 16 July 2014
Received in revised form
20 August 2014
Accepted 30 August 2014
Available online 10 September 2014

Keywords:
Anode electrode
Complex spinel titanate
Porous flake-like structure
Lithium ion battery
Solution-combustion synthesis

ABSTRACT

In this work, we report the formation of porous $Li_2MTi_3O_8$ (M = Zn, Co) flakes (hereafter referred to as f-$Li_2MTi_3O_8$) via a facile one-step solution-combustion in less than 10 min. As anodes for rechargeable lithium-ion batteries, the synthesized f-$Li_2MTi_3O_8$ exhibits high reversible charge–discharge capacity, great cycling stability and high rate performance. These results can be attributed to the intrinsic characteristics of spinel $Li_2MTi_3O_8$ flakes, in which a porous framework could provide a diffusion space for lithium ion insertion into and extraction from the anode material, resulting in excellent cycle performance, even cycling at high rate of 2000 mA g^{-1}.

1. Introduction

Compared with the conventional graphitic carbon anode materials, spinel $Li_4Ti_5O_{12}$ (LTO) exhibits a relatively flat and high lithium insertion/extraction voltage at approximately 1.55 V (*vs* Li^+/Li), much higher than the operating voltage of graphitic anodes (about 0.1 V); thus, the formation of solid-electrolyte interphase (SEI) layers and the electroplating of lithium can be avoided [1–4]. However, the LTO electrodes suffered from low theoretic capacity of 175 mA h g^{-1}, which may prevent it from large-scale applications.

More recently, the spinel structure $Li_2MTi_3O_8$ (M = Zn, Co) has attracted increasing attention for lithium ion batteries because of its high specific lithium storage capacity and cycling stability. $Li_2CoTi_3O_8$ [5,6] and $Li_2ZnTi_3O_8$ [7] are both cubic structures with similar lattice constants. H. Kawai et al. reported that bulk $Li_2CoTi_3O_8$ exhibits higher reactivity than $Li_2MgTi_3O_8$ and $Li_2ZnTi_3O_8$ towards lithium insertion [6]. Hong et al. [8] reported the fabrication and application of multi-component compounds of $Li_2MTi_3O_8$ (M = Co, Zn) using titanate nanowires as a precursor. Wang et al. [7] synthesized $Li_2CoTi_3O_8$ fibers by an electrospinning method. And in

* Corresponding author. Tel./fax: +86 5922186935.
E-mail address: jbzhao@xmu.edu.cn (J. Zhao).

http://dx.doi.org/10.1016/j.jpowsour.2014.08.129
0378-7753/

order to improve the electrical conductivity, Xu et al. [9] presented a sol–gel route to prepare $Li_2ZnTi_3O_8$/C nanocomposite. Most of the existing techniques, however, require multi-step and laborious procedures as well as are only applicable to certain predecessor.

Different from these studies, we succeeded in synthesizing $Li_2MTi_3O_8$ (M = Zn, Co) flake particles (f-$Li_2MTi_3O_8$) by a one-step solution-combustion. To the best knowledge, there has been no report on the preparation of flake $Li_2MTi_3O_8$ using combustion method. And compared with conventional synthesis methods, this route is easy to control, and has two special advantages at least: (1) one-step heating treatment shortens the reaction time and resultantly reduces the energy cost; (2) combustion synthesis in liquid phase ensures excellent homogeneity of the product with a high surface area [10–12]. The morphology, crystal structure, and electrochemical properties of the as-prepared $Li_2MTi_3O_8$ (M = Co, Zn) electrodes were investigated in detail. The results of electrochemical measurements indicate that such $Li_2MTi_3O_8$ (M = Co, Zn) anode material with porous flake-like structure exhibits an excellent cycling stability and high rate capability.

2. Experimental section

2.1. Synthesis

The f-$Li_2ZnTi_3O_8$ powders were prepared by solution-combustion synthesis using titanyl nitrate [$TiO(NO_3)_2$] aqueous solution, $Zn(NO_3)_2$ and $LiNO_3$ as the oxidant precursors and glycine as the fuel with the stoichiometric amounts of titanyl nitrate (0.0362 mol), 1.67 g of $LiNO_3$ (0.0241 mol), 3.57 g of $Zn(NO_3)_2{\cdot}6H_2O$ and 3.00 g of glycine (0.400 mol). The amount of fuel needed (stoichiometry) can be derived from the valency of the ions. In our work, the oxidizer/fuel ratio is determined by the previous reports [13]. The synthesis of [$TiO(NO_3)_2$] aqueous solution is described as followed. The transparent titanyl nitrate solution was prepared by adding nitric acid into $TiO(OH)_2$ under continuous stirring. Here $TiO(OH)_2$ was synthetized in advance by slowly dropping tetrabutyltitanate [$Ti(C_4H_9O)_4$] into dilute ammonia solution under ice-water bathing with vigorous stirring to precipitate. Stoichiometric amount of $LiNO_3$ was then added to the achieved solution, followed by the introduction of glycine as the fuel. Afterward the mixed solution was taken in an alumina crucible, placed into a muffle furnace preheated to 800 °C to sinter for 10 min. Then the reaction crucible was removed from the furnace and cooled naturally in the atmosphere.

The f-$Li_2CoTi_3O_8$ particles were prepared via the similar route but with 3.49 g of $Co(NO_3)_2$ (0.0120 mol) instead of $Zn(NO)_3{\cdot}6H_2O$.

The b-$Li_2ZnTi_3O_8$ particles were prepared via the similar route with the f-$Li_2ZnTi_3O_8$ but without the glycine as the burning agent. And the b-$Li_2CoTi_3O_8$ were prepared via the similar route with the f-$Li_2CoTi_3O_8$ but without the glycine as the burning agent.

2.2. Characterization

The X-ray diffraction (XRD) patterns were recorded with Philips X'pert Pro Super X-ray diffractometer and CuKα radiation. The X-ray photoelectron spectroscopy (XPS) analysis was performed with QUANTUM 2000 SCANNING ESCA MICROPROBE spectrometer using a focused monochromatized AlKα radiation (1486.6 eV). The pass energy was 60 eV for the survey spectra and 20 eV for particular elements. The morphologies of the as-prepared materials were characterized by field emission scanning electron microscope (LEO 1530, HITACHI S-4800). The specific surface area of porous $Li_2MTi_3O_8$ (M = Zn,Co) was measured by the Brunauer–Emmett–Teller (BET) method using nitrogen adsorption and desorption isotherms on a Tristar 3000 system.

2.3. Electrochemical characterizations

Electrochemical evaluations were carried out by galvanostatic cycling the electrodes which were constructed with the as-prepared LTO samples in a CR2016-type coin cell. The working electrodes were formed by casting the slurry, which is composed of 80 wt% active materials, 10 wt% carbon black, and 10 wt% polyvinylidene fluorides (PVDF) dissolved in N-methylpyrrolidinone (NMP) onto aluminum current collector foil. Afterward, the electrodes were dried under vacuum at 110 °C for 12 h. The cells were assembled with the cathodes as above prepared, and lithium metal as anodes. The electrolytes contained 1 mol L^{-1} $LiPF_6$ solution in a 1:1 (v:v) mixture of ethylene carbonate (EC) and dimethyl carbonate (DMC). All assembly processes of the test cells were carried out in an argon-filled glove box. Galvanostatic charge/discharge experiments were performed at different current densities between 0.02 V and 3.00 V (*vs* Li/Li^+) using a CT2001A cell test instrument (LAND Electronic Co.). The electrochemical impedance spectra (EIS) of the $Li_2MTi_3O_8$ (Zn, Co) electrodes discharged at different voltages were measured in the frequency range of 10 mHz–100 kHz by using two-electrode coil cells with Li metal as the counter electrode via an Autolab PGSTAT 101 cell test instrument.

3. Results and discussion

Fig. 1 shows XRD patterns of the as-prepared f-$Li_2MTi_3O_8$ (M = Zn, Co). All the diffraction peaks in Fig. 1a can be indexed to a cubic spinel structure of $Li_2ZnTi_3O_8$ (JCPDS No. 86-1512). Nine main characteristic peaks for $Li_2MTi_3O_8$, 2Θ = 14.9, 18.3, 27.2, 26.1, 30.2, 35.5, 43.2, 57.1, 62.5 marked by their indices 110, 111, 210, 211, 220, 311, 400, 511, 440. Since both of the samples have the spinel structures with very close lattice parameters, the similar diffraction peaks with higher crystalline can be found in Fig. 1b, which can be indexed to $Li_2CoTi_3O_8$ of space group $P4_332$ (JCPDS No. 89-1309).

SEM images of f-$Li_2ZnTi_3O_8$ and f-$Li_2CoTi_3O_8$ are shown in Fig. 2. Both of the samples prepared via the combustion method exhibit micron-size secondary particles composed of nanometer-size primary particles in flaky morphology with embedded pores, which is obtained because of concomitant formation of material with vigorous evolution of large volume of gases during the combustion reaction. And the formation reason of flake structure can be explained from the following aspects: 1) In our experiment, we have observed a vigorous reaction similar to the explosion at around 250 °C (the decomposition temperature of the glycine is 248 °C). It indicates the crystal growth in this route is fast and the volume expansion is momentary. As a consequence, the irregular flakes tend to be formed rather than the specific morphology. 2) In theory, there is not only redox reaction but also complexation between glycine and metal salts during the solution combustion [14]. Therefore, we hypothesize that the flake morphology maybe associated with the way of complexation. For the two samples, the high magnification images shown in Fig. 2e end f indicate a unique architecture containing agglomeration of uniform particles. And compared with the f-$Li_2ZnTi_3O_8$, the f-$Li_2CoTi_3O_8$ was formed by the smaller grains (about 100 nm).

Nitrogen adsorption experiment was carried out to evaluate the specific surface areas of the as-prepared f-$Li_2MTi_3O_8$ (M = Zn, Co) flake particles. As shown in Fig. 3, BET surface areas were 6.2 and 7.8 m^2 g^{-1} for f-$Li_2ZnTi_3O_8$ and f-$Li_2CoTi_3O_8$ flake particles, respectively, through calculation from N_2 isotherms at 77 K. And there is limited meso-pore (pores 2 and 8 nm) for both samples. The as-obtained samples have appreciable BET surfaces than micron-materials though in micrometer scale, which will be helpful to enhance the electrochemical performance because of their high

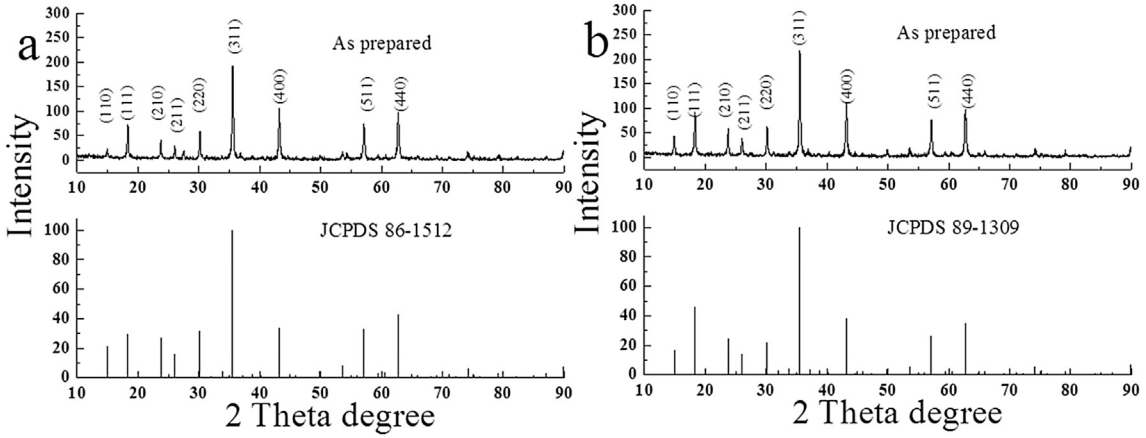

Fig. 1. XRD patterns of (a) the f-$Li_2ZnTi_3O_8$ and (b) f-$Li_2CoTi_3O_8$.

surface-to-volume ratio and short path length for Li^+ transport. And the averaged pore volumes observed for the samples using the BJH method are 2.7 and 2.8 $\times$ 10^{-2} cm^3 g^{-1} for f-$Li_2ZnTi_3O_8$ and f-$Li_2CoTi_3O_8$, respectively. From the figure, we can also see the adsorption and desorption curves separated at low and middle zone but closed at high pressure zone. This hysteresis may be attributed to the slits, which resulted from the accumulation of the flake particles [15].

As shown in Fig. 4, the f-$Li_2ZnTi_3O_8$ electrode exhibited a discharge capacity of 351 mA h g^{-1} at the first cycle (Fig. 4a), while 321 mA h g^{-1} was obtained for the $Li_2CoTi_3O_8$ (Fig. 4b). And capacities of 236 and 224 mA h g^{-1} were observed for the two different samples at the second discharge (Fig. 4a and b), respectively. (The irreversible capacity at the first cycle can probably be accounted for the formation of a surface electrolyte interface (SEI) due to the reduction of unstable species in electrolyte at low

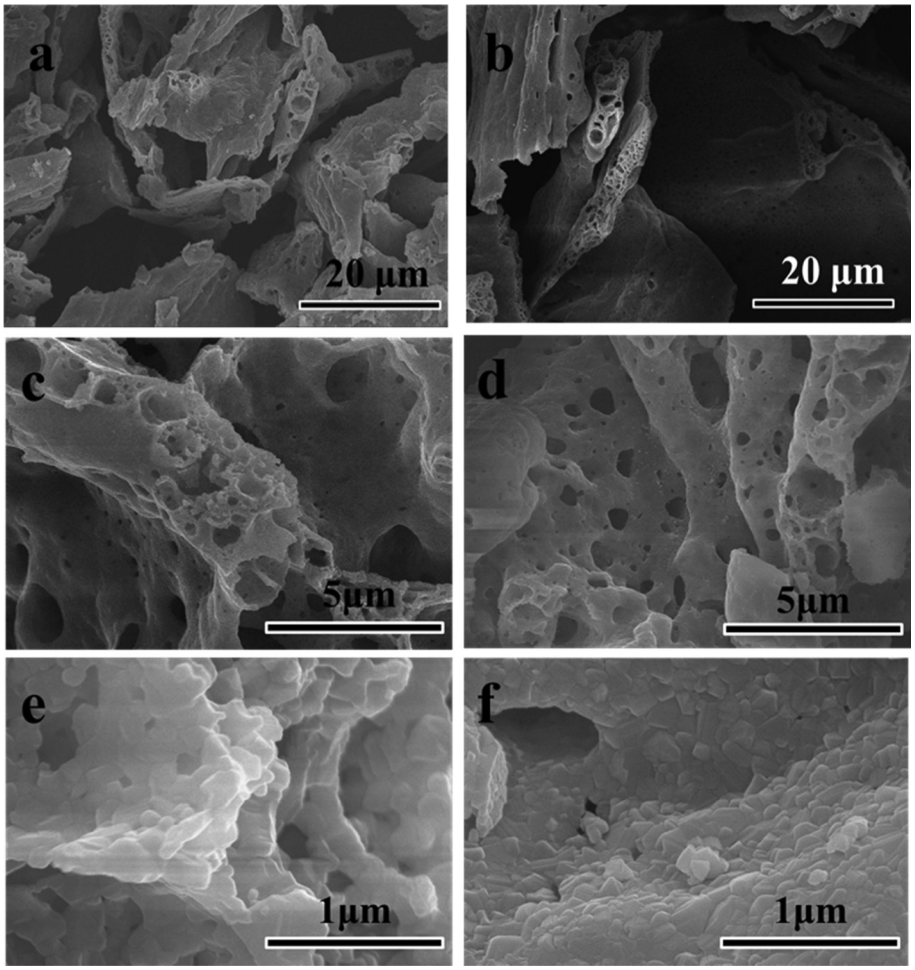

Fig. 2. SEM images of (a) f-$Li_2ZnTi_3O_8$ and (b) f-$Li_2CoTi_3O_8$. Magnified SEM images of (c, e) f-$Li_2ZnTi_3O_8$ and (d, f) f-$Li_2CoTi_3O_8$.

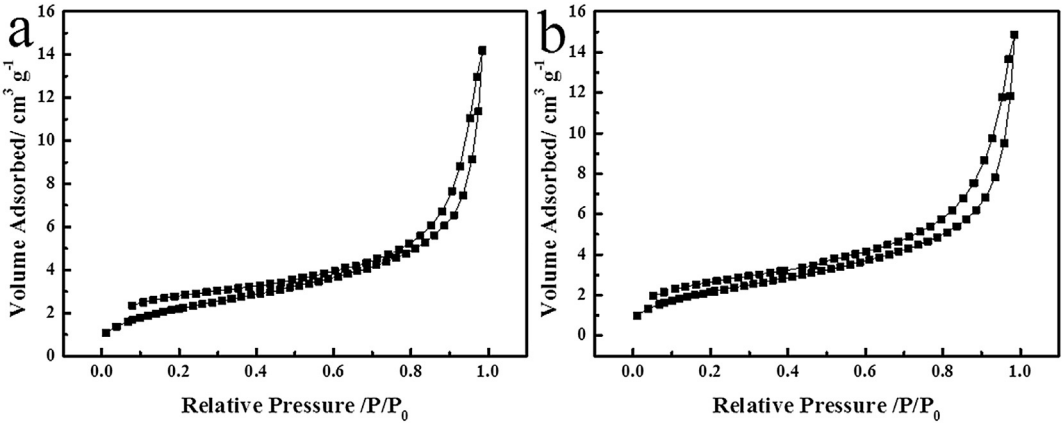

Fig. 3. Nitrogen adsorption–desorption isotherms at 77 K of (a) f-$Li_2ZnTi_3O_8$ and (b) f-$Li_2CoTi_3O_8$.

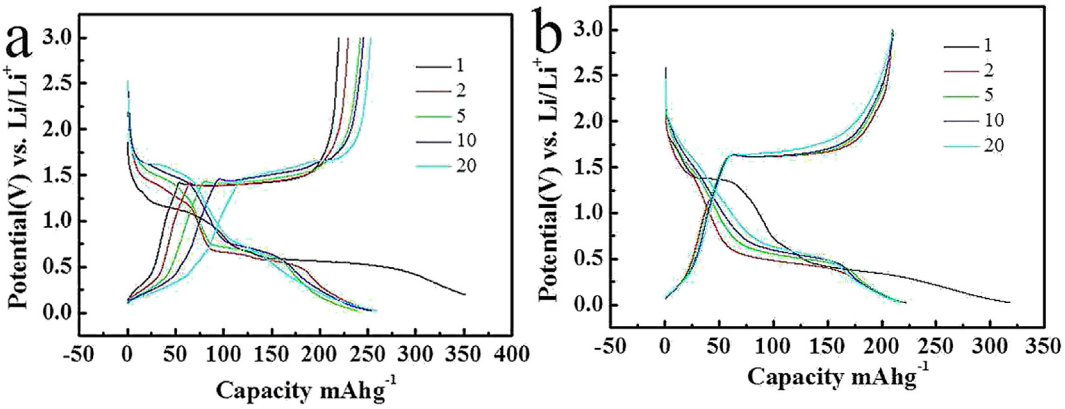

Fig. 4. Charge–discharge profiles of (a) f-$Li_2ZnTi_3O_8$ and (b) f-$Li_2CoTi_3O_8$ flake electrodes.

potential below 0.8 V (*vs* Li^+/Li) [16]). It was obvious that the increased discharge capacity for the f-$Li_2ZnTi_3O_8$ mainly occurred at the plateau region at 0.5 V. And the anode made of the f-$Li_2CoTi_3O_8$ exhibited higher reversibility towards lithium insertion and enhanced electrochemical lithium storage than the f-$Li_2ZnTi_3O_8$.

To evaluate the cycling stability of the f-$Li_2MTi_3O_8$ (M = Zn, Co) flake particles electrodes, a current density of 100 mA g^{-1} was used. As shown in Fig. 5, both of the samples exhibited excellent cycling stability. For the f-$Li_2ZnTi_3O_8$ electrode, a capacity of 192 mA h g^{-1} could be retained after 200 cycles with a capacity retention of 81%, much higher than the theoretic capacity of LTO. In the case of the f-$Li_2CoTi_3O_8$ electrode, it delivered 201 mA h g^{-1} with a high capacity retention of 89% after 200 cycles.

Fig. 6 shows the comparison of the rate capabilities between the f-$Li_2ZnTi_3O_8$ and f-$Li_2CoTi_3O_8$ electrodes at different current rates, and each sustained for 200 cycles. The f-$Li_2CoTi_3O_8$ electrodes showed considerably higher reversible capacities than the f-$Li_2ZnTi_3O_8$ electrodes at all current rates. As observed from these data, the f-$Li_2CoTi_3O_8$ showed excellent capacity retention irrespective of the rate applied. It is worth noting that more than 100 mA h g^{-1} can

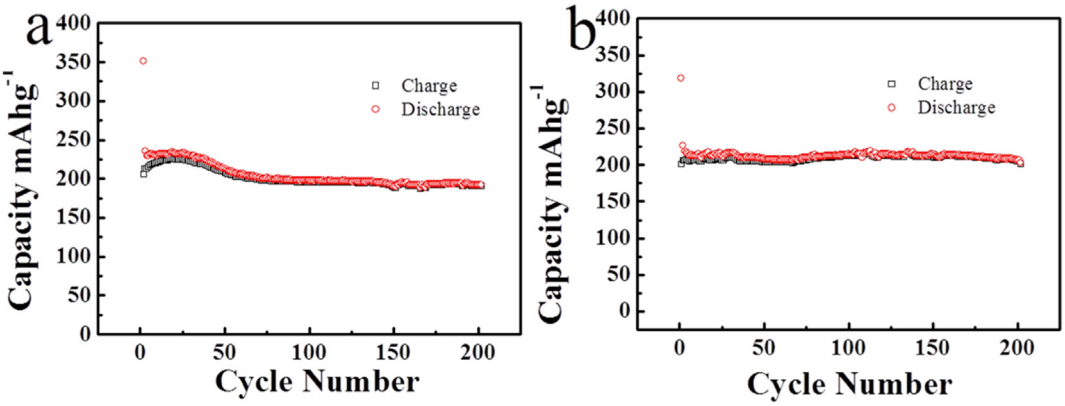

Fig. 5. Cycle performance for (a) f-$Li_2ZnTi_3O_8$ and (b) f-$Li_2CoTi_3O_8$ electrodes for 200 cycles at low capacity rate of 100 mA g^{-1}.

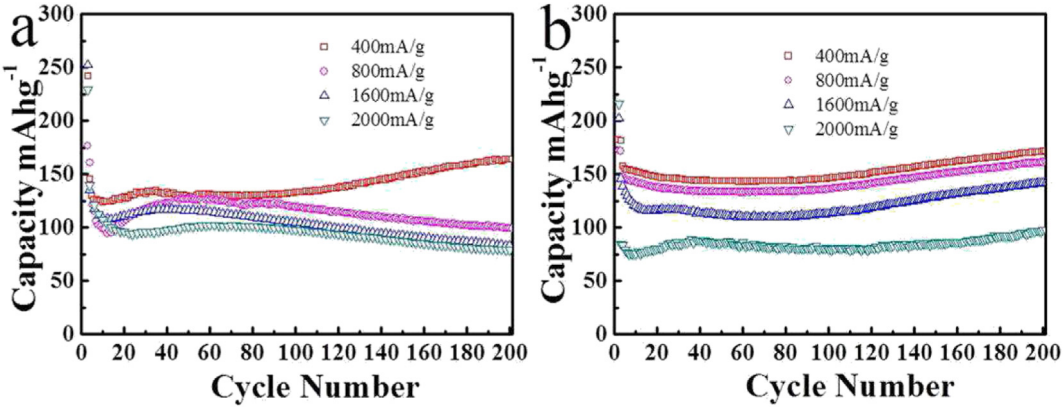

Fig. 6. Capacity *vs* cycle number plots for (a) f-$Li_2ZnTi_3O_8$ and (b) f-$Li_2CoTi_3O_8$ electrodes for 200 cycles at different discharge current rates.

Table 1
The capacities for f-$Li_2MTi_3O_8$ (M = Zn, Co) and b-$Li_2MTi_3O_8$ (M = Zn, Co) at different current rates.

Current rate (mA g^{-1})	400	800	1600	2000
f-$Li_2ZnTi_3O_8$ (mAh g^{-1})	164	100	74	73
f-$Li_2CoTi_3O_8$ (mAh g^{-1})	175	161	141	101
b-$Li_2ZnTi_3O_8$ (mAh g^{-1})	152	115	58	45
b-$Li_2CoTi_3O_8$ (mAh g^{-1})	166	137	90	64

be retained after 200 cycles even at the current rate of 2000 mA g^{-1}. It's really interesting to observe the gradual increase of the reversible capacity after 100 cycles at the rate of 400 mA g^{-1} for f-$Li_2ZnTi_3O_8$ electrode. This feature has also been previously observed for many metal oxides, suggested to be associated with the unique textural characteristics. In this work, the capacity values become larger gradually at almost all high rate in the first few cycles. It can be attributed to the slow electrolyte infiltration at higher rate for the porous surface. And this phenomenon is limited due to the incapability of retaining the porous structure. Based on the consideration of the above, we believe that the porous structure can be only retaining for a long time at rate of 400 mAh g^{-1} for f-$Li_2ZnTi_3O_8$ but retaining for a long time at almost all rates for f-$Li_2CoTi_3O_8$, which indicates the f-$Li_2CoTi_3O_8$ is superior to f-$Li_2ZnTi_3O_8$ in electrochemical reversibility. Compared with the mesoporous structure [17], the positive the positive impact can be retaining for over long term cycling (>50 cycles), which may benefit from the micron-sized pores distribution on the surface. Finally, the excellent rate performance may be attributed to the special porous flake structure. In order to verify this assumption, we have prepared bulk $Li_2MTi_3O_8$ (M = Zn, Co) (hereafter referred to as b-$Li_2MTi_3O_8$), prepared under the same condition but without glycine as combustion improver. And the XRD, SEM and electrochemical performance data are shown in Fig. S1–S4, respectively. As seen from the Fig. S1 and S2, the b-$Li_2MTi_3O_8$ in high crystalline with the size of 1–2 μm were obtained without porous flake structure, which are ten times size of the f-$Li_2MTi_3O_8$ particles. As shown in Fig. S3, we can see the cycle stability of b-$Li_2MTi_3O_8$ is lower than f-$Li_2MTi_3O_8$, only 170 and 172 mAh g^{-1} could be retained after 200 cycles for f-$Li_2ZnTi_3O_8$ and f-$Li_2CoTi_3O_8$ electrodes. We also compare the rate performance at different current density, as shown in Fig. S4 the b-$Li_2MTi_3O_8$ showed the lower rate capacities compared with the f-$Li_2MTi_3O_8$, especially at a high current rate of 2000 mA g^{-1}. A detailed comparison of each rate capacities obtained for $Li_2MTi_3O_8$ flake and bulk particles were summarized in Table 1.

In order to gain further insight into the electrochemical performance, CV measurement was carried out to characterize the electrochemical behavior of the f-$Li_2MTi_3O_8$ (M = Zn, Co) electrodes, and the results were shown in Fig. 7. In the initial cycle of the f-$Li_2ZnTi_3O_8$ electrode, two cathodic peaks appeared at 0.4 and 1.1 V, which were shifted to 0.6 and 1.3 V in the subsequent cycles (Fig. 7a). This might be related to the phase transition between spinel and roc-salts [12,18]. And a reduction peak at 0.4–0.5 V was detected for the second and subsequent cycles. This might be attributed to the multiple restoration of Ti^{4+}, which is in agreement with the previous reports [9,19,20]. In addition, there is an anodic peak at 1.5 V, which is associated with the conversion of Ti^{+4}/Ti^{+3},

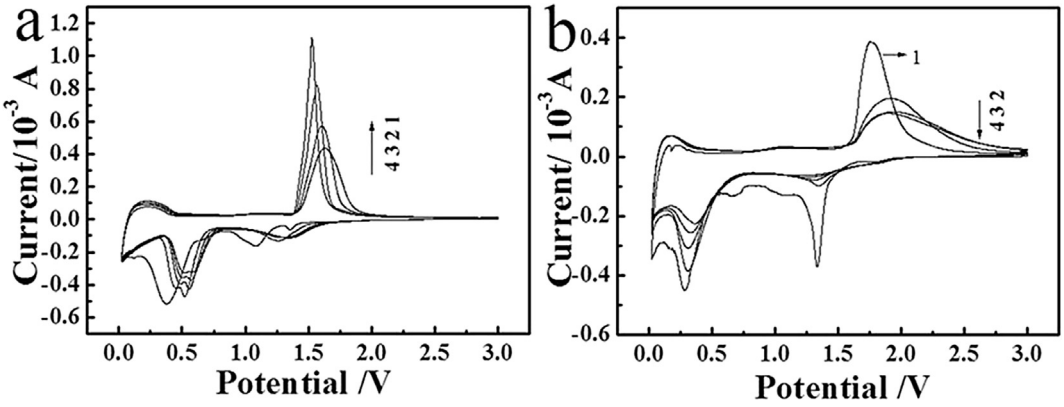

Fig. 7. CV curves of the electrodes made of (a) f-$Li_2ZnTi_3O_8$ and (b) f-$Li_2CoTi_3O_8$ particles in the voltage range of 0.05–3.0 V at a scan rate of 0.2 mV s^{-1}.

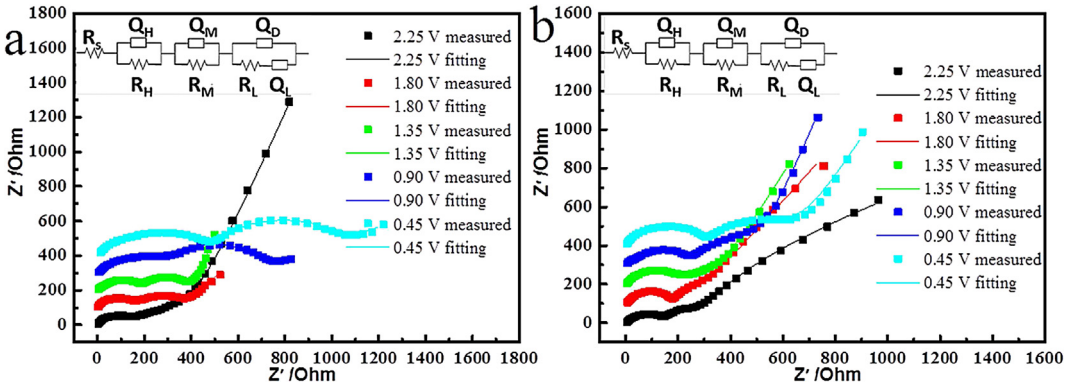

Fig. 8. Nyquist and fitting plots of (a) the f-$Li_2ZnTi_3O_8$ and (b) f-$Li_2CoTi_3O_8$ electrodes at a series of potentials in the initial discharge process.

Table 2
The equivalent circuit parameters obtained from a fit of the experimental impedance spectra of the first discharge process.

Voltage (V)	2.25 V	1.80 V	1.35 V	0.90 V	0.45 V
R_S (Ω)	1.1	1.4	8.6	79.5	176.0
R_H (Ω)	102.8	139.0	21.8	325.4	446.4
Q_H	7.2E-06	5.4E-06	3.1E-06	1.7E-06	7.2E-06
R_M (Ω)	24.4	233.3	217.0	205.2	496.8
Q_M	8.8E-07	5.4E-04	5.3E-04	4.7E-04	5.6E-04
R_L (Ω)	313.0	256.0	161.6	376.1	364.5
Q_D	4.7E-04	2.2E-04	2.7E-04	4.6E-04	6.2E-04
Q_L	1.4E-04	1.9E-08	1.1E-05	2.6E-06	1.8E-05
Voltage (V)	2.25 V	1.80 V	1.35 V	0.90 V	0.45 V
R_S (Ω)	1.2	100.6	305.4	107.8	144.5
R_H (Ω)	9.2	174	186.2	283.6	304.4
Q_H	1.90E-11	7.30E-06	1.20E-05	3.80E-05	5.50E-06
R_M (Ω)	99.1	66.0	176.0	215.2	344.4
Q_M	1.8E-05	9.7E-04	1.2E-03	9.2E-04	8.1E-04
R_L (Ω)	1.1	2.6	1.7	1.2	2.6
Q_D	8.3E-04	2.9E-03	3.5E-03	3.7E-06	9.8E-03
Q_L	2.9E-04	7.2E-07	8.8E-05	4.0E-03	1.1E-05

and then was shifted to high voltage with weaker intensity during subsequent cycles, suggesting a possible polarization process in the electrode material. For the f-$Li_2CoTi_3O_8$ electrode (Fig. 7b), in the second and subsequent cycles, all redox peaks were located at ca. 0.4/1.9 V corresponded to the conversion of Ti^{4+}/Ti^{3+}, indicating that Li^+ intercalation/deintercalation into/out of the spinel f-$Li_2CoTi_3O_8$ anode was more highly reversible than that of the f-$Li_2ZnTi_3O_8$ electrode.

To gain more information of the electrode kinetics, impendence spectra and the fitting datas of f-$Li_2ZnTi_3O_8$ and f-$Li_2CoTi_3O_8$ half cells were recorded as shown in Fig. 8 and Table 2. The Nyquist plots of f-$Li_2ZnTi_3O_8$ anode at the discharge potential (2.25 V) shows a depressed semicircle in the high-frequency range and a slightly inclined line in the low-frequency region (Fig. 8a). Once discharging at/or below 1.80 V, a new depressed semicircle appears in the medium-frequency range, and the diameter of the two semicircles increases rapidly along with the discharge process (Fig. 8a). The similar phenomenon has been reported for $Li_4Ti_5O_{12}$ anode [21]. For the f-$Li_2CoTi_3O_8$ anode, there is only one semicircle in the high-frequency range above 1.35 V (Fig. 8b). Once discharging below 1.35 V, a depressed semicircle additionally appears in the medium-frequency range, and the diameters of both semicircles increase slightly during the discharge process (Fig. 8b). At high frequencies, the semicircles are nearly identical (Fig. 8b), as they probably correspond to the passivation-film impedance on the Li metal surface. The second semicircle in the middle-frequency range is generally attributed to the charge–transfer impedance [22–24]. In comparison with the f-$Li_2ZnTi_3O_8$ electrode, the impedance for the f-$Li_2CoTi_3O_8$ electrode is largely reduced, especially the charge-transfer impedance, which can account for the improved electrochemical performance of the f-$Li_2CoTi_3O_8$ electrode.

To understand the electrochemical reaction mechanism of the f-$Li_2ZnTi_3O_8$ and f-$Li_2CoTi_3O_8$, electrodes recovered from cells in the different discharged or charged state were subjected to ex-situ XRD analysis. As shown in Fig. 9, the crystal structure of spinel f-$Li_2MTi_3O_8$ (M = Zn, Co) was not destroyed and no impurity phase was detected during the discharge process in the first cycle. As the voltage decreased, the (311) peak shifted towards lower angles in the 2θ angular position. And the crystalline interplanar spacing for the (311) peak is displayed in Table 3. Such a small shift in the peak position may result from lithium ion intercalation. These results indicate that the structures of the f-$Li_2MTi_3O_8$ (M = Zn, Co) retained significantly stability during lithium ion intercalation into and deintercalation from the electrode materials.

As shown in Fig. 10, both of the electrodes become discolored during the initial discharge process, the progressive change in color is directly correlated with the reversible occupation and de-occupation of Ti 3d orbitals (t_{2g}^1) during the electrochemical intercalation of lithium into anode. The similar phenomenon for $Li_4Ti_5O_{12}$ anode has been reported [25,26]. When charged to the original voltage, the color became shallow again. This color restoration is further indicating that the electrochemical process is reversible for the $Li_2MTi_3O_8$ (M = Zn, Co) electrodes.

4. Conclusion

In summary, an efficient synthesis approach, solution-combustion method has been developed to prepare $Li_2MTi_3O_8$ (M = Zn, Co) flake particles in one step for lithium storage application. At a current density of 100 mA g^{-1}, the obtained f-$Li_2ZnTi_3O_8$ and f-$Li_2CoTi_3O_8$ electrodes showed discharge capacities of 192 and 201 mA h g^{-1} with retentions of 81% and 89%, respectively. Both of the electrodes exhibited excellent capacity retentions irrespective of the rate used, even at a current density as high as 2000 mA g^{-1}. Especially, for the f-$Li_2CoTi_3O_8$ electrode, the current density of more than 100 mA h g^{-1} can be retained after 200 cycles even at the current rate of 2000 mA g^{-1}. These results indicate that the as-prepared anodes with spinel flake particles have a large reversible capacity and high rate performance, which can be attributed to the 3D porous flamework structures and their intrinsic characteristics. This special 3D porous flamework structure could provide a diffusion space for lithium-ion into and extraction from the material. In addition, the porous flamework composed of several tens of nanometers greatly decreased the diffusion distance for lithium

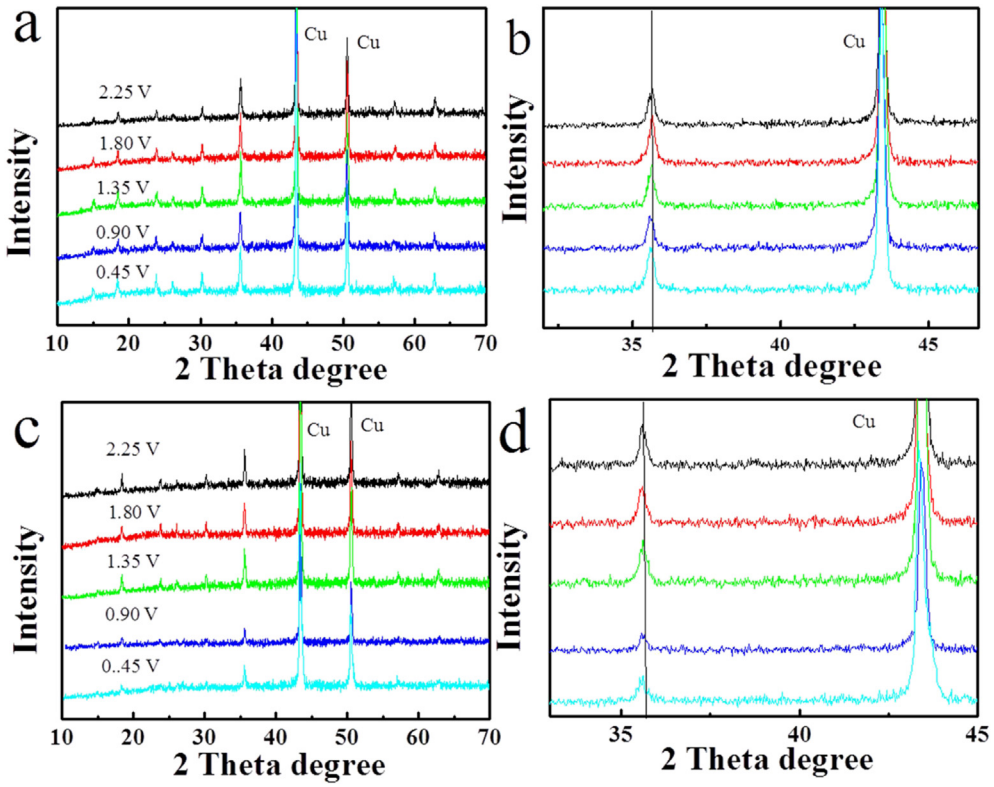

Fig. 9. Ex-site XRD patterns of the (a) f-$Li_2ZnTi_3O_8$ and (c) f-$Li_2CoTi_3O_8$ electrodes at different discharge voltages in the initial cycle, (b) the (311) peak area of f-$Li_2ZnTi_3O_8$, (d) the (311) peak area of f-$Li_2CoTi_3O_8$.

Table 3
The change of the crystalline interplanar spacing for the (311) peak during the first discharge.

Electrode	*d* (2.25 V)	*d* (1.80 V)	*d* (1.35 V)	*d* (0.90 V)	*d* (0.45 V)
f-$Li_2ZnTi_3O_8$	2.5172 Å	2.5168 Å	2.5189 Å	2.5207 Å	2.5318 Å
f-$Li_2CoTi_3O_8$	2.5177 Å	2.5178 Å	2.5183 Å	2.5213 Å	2.5337 Å

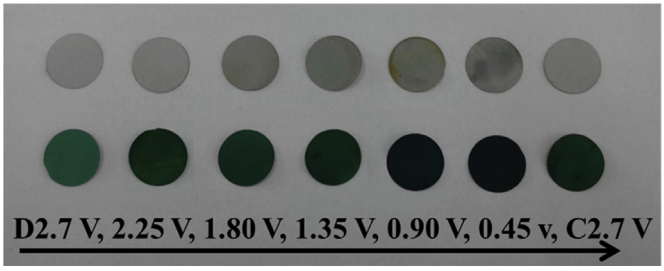

Fig. 10. Photo images of f-$Li_2ZnTi_3O_8$ (gray) and f-$Li_2CoTi_3O_8$ (green) electrodes at various potentials in the initial discharge and charge progress. (For interpretation of the references to color in this figure legend, the reader is referred to the web version of this article.)

ions and electrons in the solid state. Thus, we believe that such a facile solution-combustion method could be applied in a wide range of fields and the f-$Li_2MTi_3O_8$ (M = Zn, Co) could be promising anode materials for high-rate lithium batteries.

Acknowledgments

The authors gratefully acknowledge the financial supports from the National High Technology Research and Development Program of China (2012AA110204), the Fujian Natural Science Foundation (2012J05028) and the National Fund for Fostering Talents of Basic Science (J1210014).

Appendix A. Supplementary data

Supplementary data related to this article can be found at http://dx.doi.org/10.1016/j.jpowsour.2014.08.129.

References

[1] T. Ohzuku, A. Ueda, N. Yamamoto, J. Electrochem. Soc. 142 (1995) 1431–1435.
[2] P.G. Bruce, B. Scrosati, J.M. Tarascon, Angew. Chem. Int. Ed. 47 (2008) 2930–2946.
[3] Z.H. Chen, I. Belharouak, Y.K. Sun, K. Amine, Adv. Funct. Mater. 25 (2013) 959–969.
[4] D. Young, A. Ransil, R. Amin, Z. Li, Y.M. Chiang, Adv. Energy Mater. 3 (2013) 1125–1129.
[5] N. Reeves, D. Pasero, A.R. West, J. Solid State Chem. 180 (2007) 1894–1901.
[6] H. Kawai, M. Tabuchi, M. Nagata, H. Tukamoto, A.R. West, J. Mater. Chem. 8 (1998) 1273–1280.
[7] L. Wang, L.J. Wu, Z.H. Li, G.T. Lei, Q.Z. Xiao, P. Zhang, Electrochim. Acta 56 (2011) 5343–5346.
[8] Z.S. Hong, X.Z. Zheng, X.K. Ding, L.L. Jiang, M.D. Wei, K.M. Wei, Energy Environ. Sci. 56 (2011) 5343–5346.
[9] Y.X. Xu, Z.S. Hong, L.C. Xia, J. Yang, M.D. Wei, Electrochim. Acta 88 (2013) 74–78.
[10] T. Yuan, K. Wang, R. Cai, R. Ran, Z.P. Shao, J. Alloys Compd. 447 (2009) 665–672.
[11] M.W. Raja, S. Mahanty, M. Kundu, R.N. Basu, J. Alloys Compd. 468 (2009) 258–262.
[12] A.S. Prakash, P. Manikandan, K. Ramesha, M. Sathiya, J.M. Tarascon, A.K. Shukla, Chem. Mater. 22 (2010) 2857–2863.
[13] X. Li, H.C. Lin, W.J. Cui, Q. Xiao, J.B. Zhao, ACS Appl. Mater. Interfaces 6 (2014) 7895–7901.
[14] M. Lackner, Combustion Synthesis: Novel Routes to Novel Materials, vol. 1, Bentham Science Publisher, 2010, pp. 3–4.
[15] S.J. Gregy, K.S. Sing, Adsorption, Surface Area and Porosity, vol. 2, Academic Press, 1982, pp. 194–195.

[16] M. Stjerndahl, H. Bryngelsson, T. Gustafsson, J.T. Vaughey, M.M. Thackeray, K. Edström, Electrochim. Acta. 52 (2007) 4947–4955.
[17] K.M. Shaju, F. Jiao, A. Debart, P.G. Bruce, Phys. Chem. Chem. Phys. 9 (2007) 1837–1842.
[18] W. Lu, I. Belharouak, J. Liu, K. Amine, J. Electrochem. Soc. 154 (2) (2007) A114–A118.
[19] H. Ge, N. Li, D. Li, C. Dai, D. Wang, Electrochem. Commun. 10 (2008) 719–722.
[20] W.J.H. Borghols, M. Wagemaker, U. Lafont, E.M. Kelde, F.M. Mulder, J. Am. Chem. Soc. 131 (2009) 17786–17792.
[21] K. Wu, J. Yang, X.Y. Qiu, J.M. Xu, Q.Q. Zhang, J. Jin, Q.C. Zhuang, Electrochim. Acta. 108 (2013) 841–851.
[22] H.L. Pan, L. Zhao, Y.S. Hu, H. Li, L.Q. Chen, ChemSusChem 5 (2012) 526–529.
[23] N. Schweikert, H. Hahn, S. Indris, Phys. Chem. Chem. Phys. 13 (2011) 6234–6240.
[24] M.D. Levi, G. Salitra, B. Markovsky, H. Teller, D. Aurbach, Udo Heider, L. Heider, J. Electrochem. Soc. 146 (1999) 1729–1734.
[25] M.S. Song, A. Benayad, Y.M. Choi, K.S. Park, Chem. Commun. 48 (2012) 516–518.
[26] Q. Zhu, Y. Peng, L. Lin, C.M. Fan, G.Q. Gao, R.X. Wang, A.W. Xu, J. Mater. Chem. A 2 (2014) 4429–4437.